nature communications

Article

https://doi.org/10.1038/s41467-025-65611-4

Acoustic spin skyrmion molecule lattices enabling stable transport and flexible manipulation

Received: 21 May 2025

Accepted: 20 October 2025

Lei Liu[1], Xiujuan Zhang[1] ✉, Ming-Hui Lu[1,2,3] ✉ & Yan-Feng Chen[1,3] ✉

Skyrmions—topologically protected nanoscale spin textures with vortex-like configurations—hold transformative potential for ultra-dense data storage, spintronics and quantum computing. However, their practical utility is challenged by dynamic instability, complex interaction, and the lack of deterministic control. Here, we introduce a skyrmion molecule lattice, a novel architecture where pairs of skyrmions with opposite polarizability are symmetry-locked into stable molecule configurations. These molecules emerge as propagating eigenstates of the system, enabling robust transport. Using a boundary engineering technique, we achieve deterministic control over skyrmion creation, deformation, annihilation, and polarizability inversion. This is experimentally demonstrated in a graphene-inspired acoustic surface wave metamaterial by harnessing topological acoustic spin structures. Our work, leveraging symmetry principles, establishes a universal framework for stabilizing, transporting and manipulating the skyrmion quasiparticles.

Skyrmions, first conceptualized by Tony Skyrme in 1961 as a particle-like field model describing baryons in nuclear physics[1], were later adapted to condensed matter physics to describe topologically stable swirl or vortex-like spin configurations[2–11]. These structures cannot be smoothly deformed into magnetic ground states with uniformly aligned spins due to their nontrivial topology[8], making them robust against perturbations. This intrinsic stability, combined with their nanoscale size and controllability via external fields such as electric fields[6,7,12–14], magnetic fields[15], optical excitation[16], acoustic waves[17,18], and thermal gradients[19], positions skyrmions as transformative elements for next-generation technologies, from nonvolatile memory to neuromorphic computing. However, the practical utility of skyrmions is challenged by universal obstacles transcending specific physical systems, including dynamic instability, unpredictable nonlinear response to external stimuli, and a critical lack of deterministic control.

These challenges have motivated the exploration of skyrmions in clean, controllable classical wave systems[20–40], such as optical[20], acoustic[25] and water wave[38] systems, where they can manifest in various vector fields like electric polarization[20–24,26,30,32–34,36,40] and fluid velocity[31,38]. While these studies have significantly expanded the physical relevance of skyrmions, many realizations rely on static interference patterns from carefully tailored excitations and therefore lack the key attributes of intrinsic stability, transportability and flexible control, which are essential for practical applications. Recently, notable progress has been made. For instance, acoustic Archimedes metastructures have been proposed to generate localized skyrmions without tailored excitations[28,29,35,39]. Highly flexible optical retarder arrays now enable on-demand skyrmion generation[40]. Theoretically, novel frameworks extend skyrmion topology beyond conventional skyrmion-number descriptions, revealing mechanisms for both global and local topological protection[36,37]. Despite these advances, however, achieving all desired attributes—stability, transportability, and control—in a comprehensive manner remains an open challenge.

In this work, we introduce the skyrmion molecule lattice, a material-agnostic, symmetry-enforced platform, to unite all three virtues. The platform consists of a periodic array of bound skyrmion pairs with complementary polarizability, stabilized by lattice symmetry and enabling robust transport and deterministic control. As illustrated in

---

[1]National Laboratory of Solid State Microstructures and Department of Materials Science and Engineering, Nanjing University, Nanjing, China. [2]Jiangsu Key Laboratory of Artificial Functional Materials, Nanjing, China. [3]Collaborative Innovation Center of Advanced Microstructures, Nanjing University, Nanjing, China. ✉e-mail: xiujuanzhang@nju.edu.cn; luminghui@nju.edu.cn; yfchen@nju.edu.cn

Fig. 1, our approach leverages the interplay between lattice symmetry and anisotropic *p*-orbitals. By strategically arranging the orbitals within a graphene-like lattice, we generate a pair of vortices with opposite chirality at different sublattice sites. These vortices are intrinsically locked to the K and K' valleys and symmetry-protected, forming a stable vortex molecule. Embedding this vortex molecule lattice into evanescent fields couples the out-of-plane vortex spin with the in-plane spin of the evanescent field, generating a full 3D spin vector field and thereby realizing the spin skyrmion molecule lattice. Crucially, these skyrmion molecules emerge as propagating eigenstates of the system, enabling robust transport with minimal scattering. Furthermore, we develop a boundary engineering technique that allows for the precise manipulation of these molecules—including their creation, deformation, annihilation, and polarizability inversion—by tuning sample boundaries in a linear and predictable manner.

Our symmetry-based approach establishes molecule lattices as a comprehensive platform for stabilizing, transporting and controlling skyrmions in a highly tunable setting. This approach is universal and is readily transferable to other symmetry groups, higher-order orbitals, and various physical domains like photonics, gravity waves, and electronic systems, where the unique properties of each system could further enhance the functionality of topological vector textures. Looking forward, integrating with active control mechanisms (e.g., electro-acoustic, electro-optical couplings), this platform could unlock real-time, on-chip skyrmion operations for ultrafast and reconfigurable spin-wave technologies.

Results

Realization of the skyrmion molecule lattice

As illustrated in Figs. 1 and 2a, we begin with two orthogonal in-plane *p*-orbitals $|p_x\rangle$ and $|p_y\rangle$ as the basis, strategically arranging them to form a graphene-like lattice. This system is governed by transverse (t_T) and longitudinal (t_L) couplings, where t_T is negligible compared to t_L and set to $t_T = 0$ without loss of generality. In momentum space, the Hamiltonian is given by

$$H(\mathbf{k}) = \begin{bmatrix} 0_{2\times 2} & h(\mathbf{k}) \\ h^{\dagger}(\mathbf{k}) & 0_{2\times 2} \end{bmatrix}, \tag{1}$$

with

$$h(\mathbf{k}) = t_L \begin{bmatrix} \frac{3}{4}\left(e^{i\mathbf{k}\cdot\mathbf{e}_2} + e^{i\mathbf{k}\cdot\mathbf{e}_3}\right) & \frac{\sqrt{3}}{4}\left(e^{i\mathbf{k}\cdot\mathbf{e}_2} - e^{i\mathbf{k}\cdot\mathbf{e}_3}\right) \\ \frac{\sqrt{3}}{4}\left(e^{i\mathbf{k}\cdot\mathbf{e}_2} - e^{i\mathbf{k}\cdot\mathbf{e}_3}\right) & \frac{1}{4}\left(e^{i\mathbf{k}\cdot\mathbf{e}_2} + e^{i\mathbf{k}\cdot\mathbf{e}_3}\right) + e^{i\mathbf{k}\cdot\mathbf{e}_1} \end{bmatrix}. \tag{2}$$

Here, † indicates the complex conjugate transpose. The lattice constant is taken as 1, $\mathbf{k}\left(k_x, k_y\right)$ denotes the wave vector, and $\mathbf{e}_n$ ($n = 1, 2, 3$) is the lattice vector in the real space. $H(\mathbf{k})$ corresponds to the eigenfunction $\psi = \left(\phi_{\alpha,p_x}, \phi_{\alpha,p_y}, \phi_{\beta,p_x}, \phi_{\beta,p_y}\right)^T$, where ϕ_{i,p_j} ($i = \alpha, \beta$ and $j = x, y$) represents the $|p_j\rangle$ orbital component on site *i*. The strategic orbital arrangement induces distinct propagation phases for $|p_x\rangle$ and $|p_y\rangle$, yielding a total wavefunction $\Psi = |p_x\rangle + e^{i\mathscr{D}}|p_y\rangle$ at each site, where the phase difference $\mathscr{D} = \arg\left(\frac{\phi_{i,p_y}}{\phi_{i,p_x}}\right)$. Taking $t_L = 1$, the band structure incorporating $\mathscr{D}$ is shown in Fig. 2b, which inherits the unique properties of the graphene lattice and features six Dirac points at the K and K' points. At these points, $|p_x\rangle$ and $|p_y\rangle$ acquire a 90° phase difference, with $\mathscr{D} = \frac{\pi}{2}$ for site β and $\frac{3\pi}{2}$ for α at the K point, and reversed roles at the K' point due to the time-reversal symmetry. Correspondingly, the orthogonally overlapped $|p_x\rangle$ and $|p_y\rangle$ are superposed, forming circular patterns that manifest as vortices. These vortices exhibit 2π phase variation around their center, thereby carrying topological charges of ± 1. The corresponding wavefunctions are given by $\Psi_{\pm} = |p_x\rangle \pm i|p_y\rangle$. The right panel of Fig. 2b illustrates the phase distributions of $|p_x\rangle$ and $|p_y\rangle$ for eigenstates at different Dirac points. At the K point, superposition of $|p_x\rangle$ and $|p_y\rangle$ creates Ψ_- at site α and Ψ_+ at β, which are coupled with each other and locked into even and odd vortex pairs, yielding $\mathrm{M}_{K,\mathrm{even}} = \{\Psi_-, \Psi_+\}$ and $\mathrm{M}_{K,\mathrm{odd}} = \{\Psi_-, -\Psi_+\}$. We designate each of

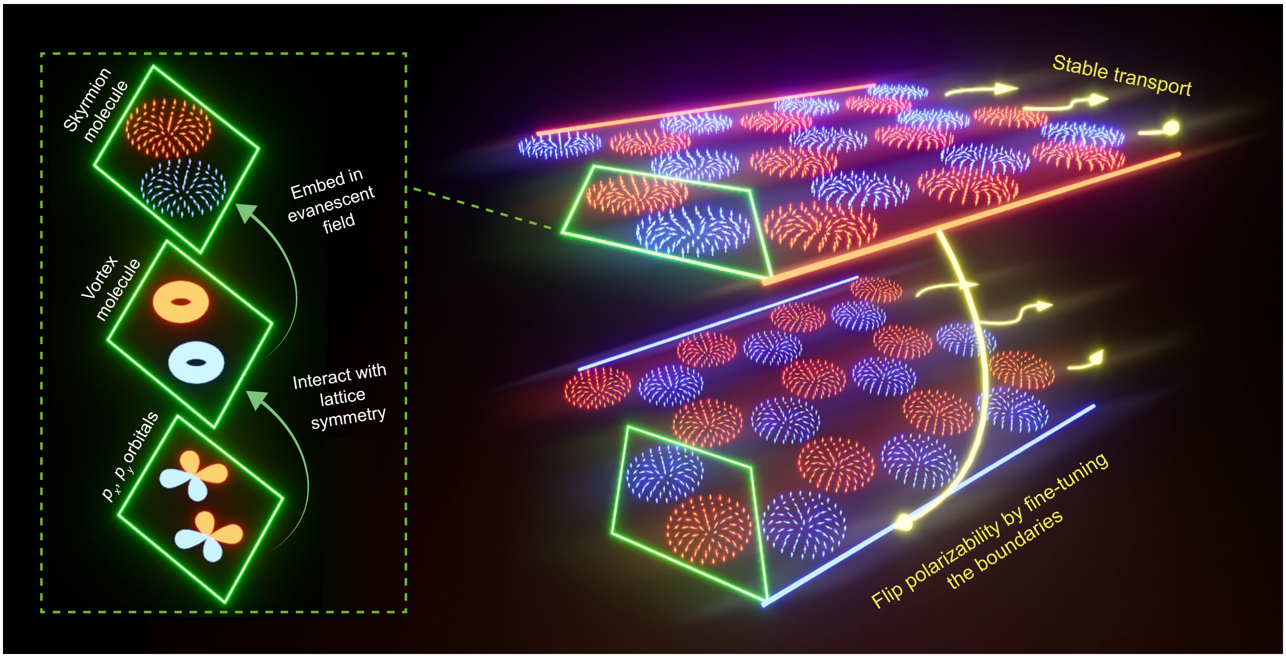

Fig. 1 | Schematic of the skyrmion molecule lattice. The left panel (outlined by the dashed box) illustrates the key steps for its realization. Two orthogonal in-pane *p*-orbitals, $|p_x\rangle$ and $|p_y\rangle$, serve as the basis to construct a graphene lattice. Each unit cell contains two sublattice sites. Enabled by graphene's lattice symmetry, $|p_x\rangle$ and $|p_y\rangle$ acquire a 90° phase difference at the Dirac points, superposing into vortices. Due to the inversion symmetry, vortices at different sublattice sites carry opposite topological charges, locked together into a neutral, stable configuration termed a vortex molecule. When coupled to an evanescent field with in-plane spin angular momentum, vortex molecules evolve into skyrmion molecules composed of symmetry-locked skyrmion pairs with opposite skyrmion numbers (see the following section for mechanistic details). As eigenstates of the system, these molecules enable stable transport and flexible control over their creation, deformation, annihilation, and even polarizability inversion by fine-tuning the material boundaries, as depicted in the right panel.

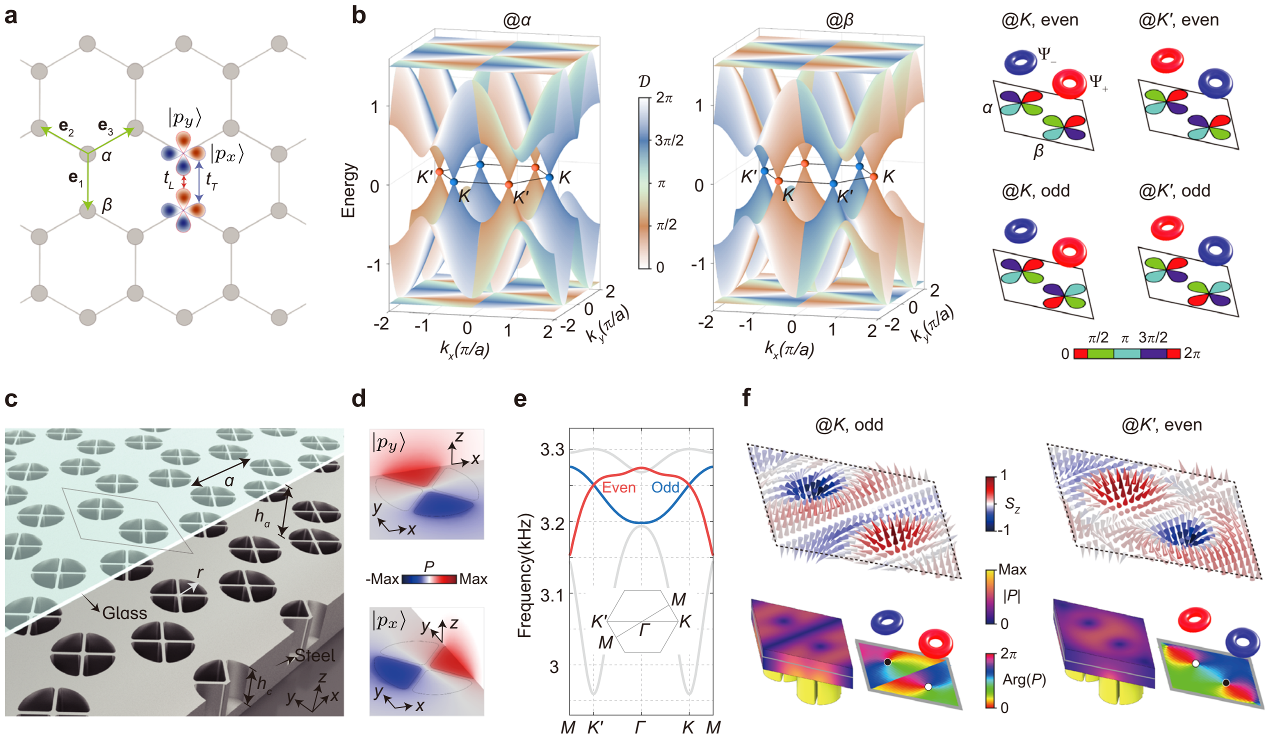

Fig. 2 | Realization of the skyrmion molecule lattice. a Schematic of the p-orbital graphene lattice. **b** Energy bands incorporating $\mathscr{D}$ (the phase difference between $|p_x\rangle$ and $|p_y\rangle$) for sublattice sites α (left) and β (middle). At the Dirac points, 90° phase difference gives rise to vortices with topological charges of ±1, yielding wavefunctions $\Psi_\pm = |p_x\rangle \pm i|p_y\rangle$. Enforced and stabilized by the inversion symmetry, these vortices couple with each other and lock into neutral molecules with even and odd parities. Right panel: Eigenstates of the vortex molecules at the K and K' Dirac points. **c**, An acoustic surface wave metamaterial implementing the lattice in **a**. Petaloid cavities are carefully etched on a steel surface to meet the graphene's symmetry requirements while providing an evanescent field. An acrylic ceiling is placed above the steel surface to confine the surface wave propagation (see Methods for detailed geometric parameters and discussions on the acrylic ceiling). **d** Acoustic pressure field distributions of the two dipole resonant modes for each petal, serving as the $|p_x\rangle$ and $|p_y\rangle$ basis. **e** Band structure of the metamaterial, which hosts Dirac points at the K and K' points, matching the theoretical prediction in **b**. **f** Normalized spin angular momentum $\hat{\mathbf{s}} = \mathbf{s}/|\mathbf{s}|$ for eigenstates at the Dirac points (upper panels). Emergence of paired vortex-like spin textures with opposite polarizability reveals the skyrmion molecules. Their symmetry correlation with the underlying vortex molecules is confirmed by the pressure field amplitudes and phase distributions (lower panels).

these vortex pairs as a molecule. At the K' point, the vortex molecules are $\mathrm{M}_{K',\mathrm{even}} = \{\Psi_+, \Psi_-\}$ and $\mathrm{M}_{K',\mathrm{odd}} = \{\Psi_+, -\Psi_-\}$ (detailed derivations are provided in the Supplementary Note 1).

It is noted that the graphene lattice possesses C_{3v}, inversion, and time-reversal symmetries at the K and K' points. Among these symmetries, it is fundamental that the inversion symmetry enforces the complementary vortex pairs (i.e., the vortex molecules), underscoring their symmetry protection and intrinsic stability. Meanwhile, the C_{3v} point-group and time-reversal symmetries primarily govern the valley characteristics, enabling valley-locked robust transport and boundary-engineering-driven mode transition (which will be discussed in the following). This establishes inversion symmetry as the key prerequisite for the core symmetry-enforced pairing mechanism, a principle that extends beyond graphene lattice and applies universally across different crystalline point groups (see Supplementary Note 1).

An in-plane vortex corresponds to a phase singularity in a scalar field, whose spatial gradient induces a rotational vector structure, manifesting as an out-of-plane spin angular momentum[41,42]. To construct a full 3D spin vector field, however, an in-plane spin component is still required. We achieve this by exploiting the evanescent field, whose in-plane and out-of-plane vector components exhibit a $\frac{\pi}{2}$ phase difference. This generates an additional rotation of the field, producing in-plane spin angular momentum[43–45]. By embedding the vortex molecule lattice into such an evanescent environment, the in-plane and out-of-plane spin components interact, resulting in a complete 3D spin vector field. Crucially, the spin vector field inherits the symmetries of the underlying lattice, forming vortex-like, stable spin texture pairs, namely, skyrmion molecules.

To implement the skyrmion molecule lattice, we design an acoustic surface wave metamaterial. As depicted in Fig. 2c, the metamaterial consists of open resonant cavities on a steel plate, forming a graphene-like lattice. Each sublattice site (α or β) comprises four petaloid cavities hosting two degenerate orthogonal p-orbital-like dipole resonant modes, as illustrated by the pressure field distributions in Fig. 2d. These resonant modes form the basis of our design and couple to each other via spoof surface acoustic waves, which are precisely evanescent fields. Figure 2e presents the band structure for this material, featuring Dirac points at the K and K' valleys. To visualize the skyrmion molecules, we show in Fig. 2f (upper panels) the distributions of the acoustic spin angular momentum, $\mathbf{s}$, for the eigenstates at these points. Here, $\mathbf{s}$ describes the rotation of the velocity vector field $\mathbf{v}$, yielding[46]

$$\mathbf{s} = \frac{\rho}{2\omega}\mathrm{Im}\left(\mathbf{v}^* \times \mathbf{v}\right), \qquad (3)$$

where ρ denotes the mass density and ω the angular frequency. It is observed that each molecule indeed contains two spin textures with oppositely swirling configurations, consistent with the typical features of two Néel-type skyrmions $\mathrm{S}_\pm$ with skyrmion numbers ±1 (see Supplementary Note 2 for calculations of the skyrmion numbers). Crucially, the skyrmion molecules strictly align with the symmetry constraints, with one-to-one correspondence to the symmetry-locked vortex molecules, adhering S_+ to Ψ_+ and S_- to Ψ_-. This is confirmed by the lower panels of Fig. 2f. When examining the scalar features, i.e., the intensity and phase distributions of the pressure field, they directly map to the underlying vortex pairs with opposite chirality. This

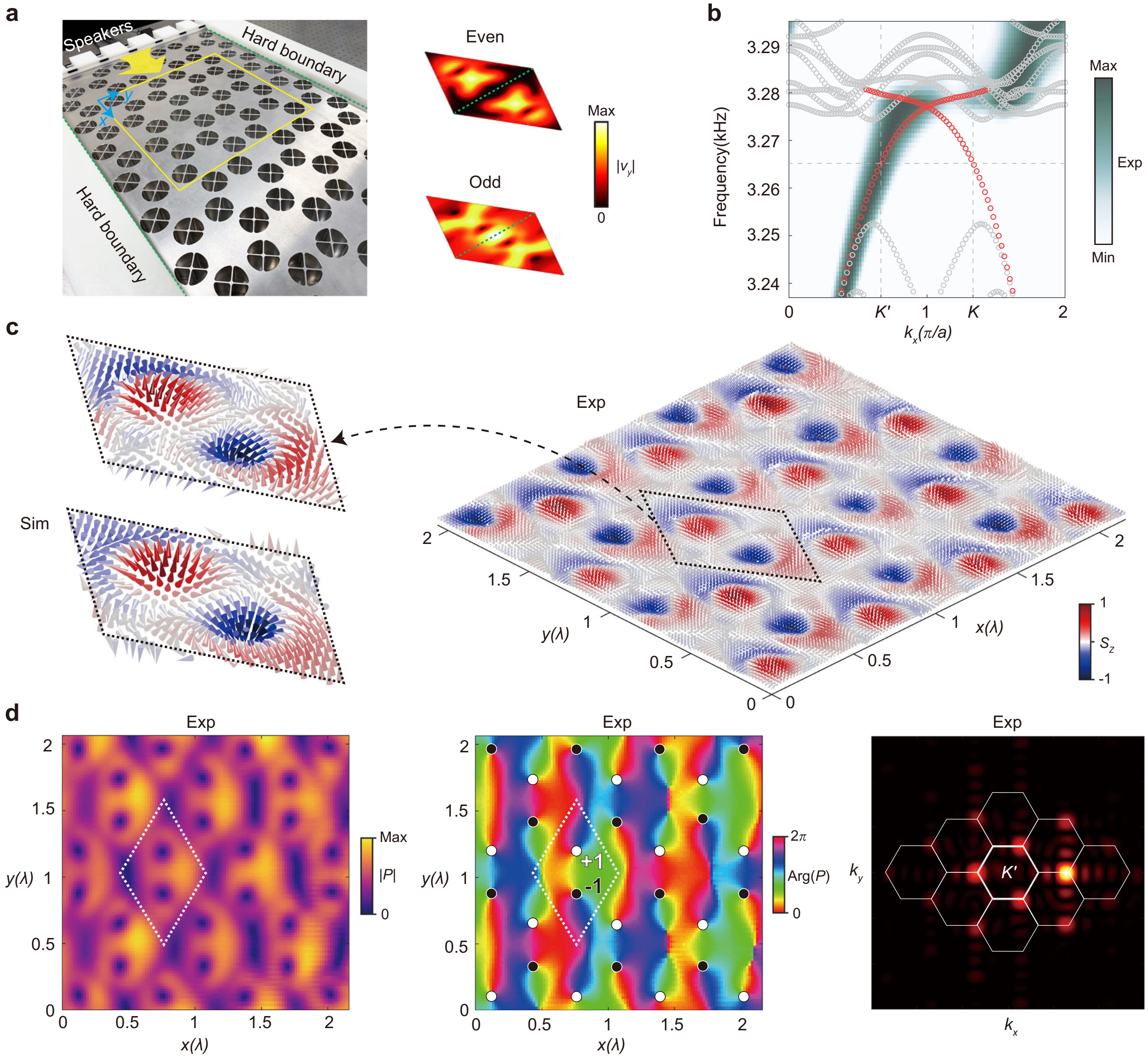

Fig. 3 | Observation of robust transport of the skyrmion molecules. a Left: Fabricated waveguide, open along the x-direction and bounded by hard boundaries along the y-direction, enforcing zero normal velocity ($|v_y| = 0$). Right: Simulated $|v_y|$ for the even and odd skyrmion molecules. The hard boundary condition admits the even molecule while suppressing the odd one. **b** Numerically calculated (circles) and experimentally measured (colormap) band structures of the waveguide, validating the boundary selection for the even molecule. **c** Measured spin vector field $\hat{\mathbf{s}} = \mathbf{s}/|\mathbf{s}|$ (the measurement region is marked by the yellow box in **a**). Regular, uniform field patterns reveal stable skyrmion molecule transport, matching the simulated eigenstate. **d** Left to right: Measured pressure amplitude $|P|$, phase Arg(P), and the Fourier spectrum. These results align with both the theoretical and numerical predictions in Fig. 2, highlighting the intrinsic correlation between the skyrmion and vortex molecule lattices and their symmetry-protected valley-locking.

correlation further highlights the critical role of symmetries in forming and stabilizing skyrmion molecules.

Here, we emphasize that the skyrmion molecule emerge from the coupling of two full skyrmions that are well separate in the real space, with topological charges equal in magnitude but opposite in sign. This constitutes a novel spin texture with zero net skyrmion number, distinct from existing quasiparticle types such as bimerons[47] skyrmioniums[48,49], or higher-order quasiparticles[32,50]. This charge-neutral, topologically compensated state is especially attractive for device applications, as it suppresses the skyrmion Hall effect, preventing unwanted transverse drift[51].

Observation of robust transport of the skyrmion molecules

Benefiting from our graphene-inspired periodic lattice design, the skyrmion molecules emerge as propagating eigenstates, carrying non-zero group velocity for stable transport. To demonstrate this, we employ boundary engineering, a technique that modulates the material boundaries to select eigenstates satisfying specific boundary conditions, analogous to an infinite potential well[52]. This method, previously used to generate defect-immune bulk states[53,54], is uniquely applied here to isolate and control the even and odd skyrmion molecules. These modes exhibit distinct parities and thus match to different boundary conditions. Figure 3a shows a fabricated waveguide bounded by hard walls along the y-direction and open along the x-direction (the transport direction). This type of waveguide is commonly used in practice. The hard boundaries enforce zero normal velocity, i.e., $|v_y| = 0$, permitting only the even skyrmion molecule that satisfies this condition, as illustrated by the velocity field distributions in the right panel of Fig. 3a. The odd mode, on the other hand, incompatible with the boundary condition, is excluded. Experimental validation is provided in Fig. 3b by the measured band

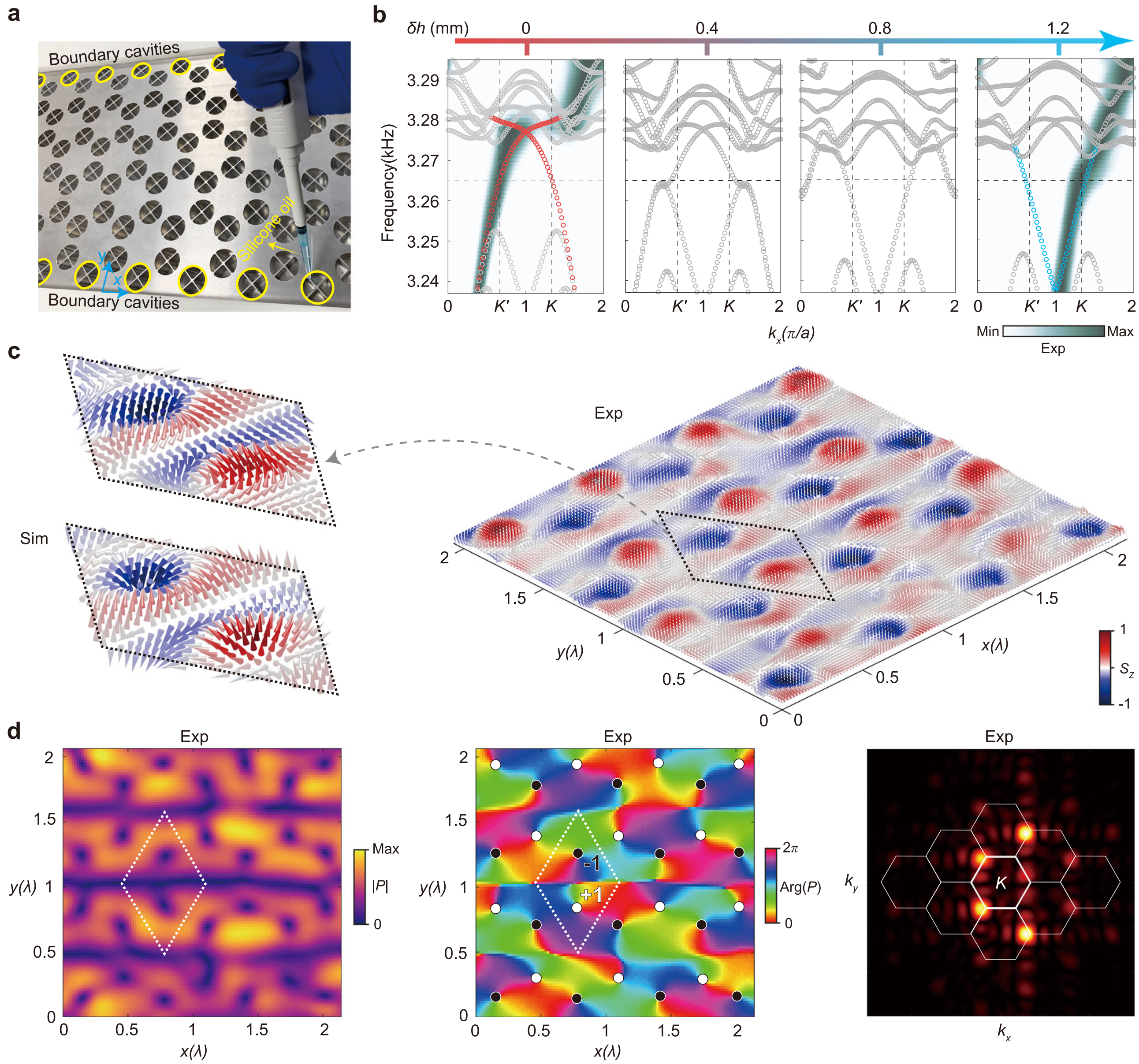

Fig. 4 | Deterministic skyrmion molecule manipulation via boundary engineering. a Boundary modulation by injecting measured amounts of silicone oil into the boundary cavities, tuning their depth. **b** Band structure evolution under cavity depth change δh. As δh increases, the even band shifts toward high frequencies, detaching from the Dirac points and causing deformation and annihilation of the even skyrmion molecules. Concurrently, the odd band emerges and intersects the Dirac points at $\delta h = 1.2$ mm, signaling the odd skyrmion molecules. **c**, **d** Measurements analogous to Fig. 3c, d, but with boundary cavities modulated by $\delta h = 1.2$ mm. Observation of skyrmion molecules $\{S_-, S_+\}$ and their vortex-like scalar features reveals polarizability inversion relative to the even molecules, validating the boundary engineering control. The Fourier spectrum retains valley-locking, affirming symmetry-protected robustness under boundary engineering.

structure for this waveguide, featuring only the even band (see Methods for the experimental set-up and measurement details).

To observe the transport of the even skyrmion molecule, we launch an excitation from the left port of the waveguide at 3.265 kHz (corresponding to the K' valley). The measured spin vector field (Fig. 3c) reveals stable, uniform $M_{K',\mathrm{even}}$ skyrmion molecules, consistent with both the theory and simulations. Their scalar features are also experimentally confirmed, as shown in Fig. 3d, where paired vortices with chirality $\{+1, -1\}$ are precisely observed. For further evidence, we conduct Fourier analysis on the measured pressure field (see Fig. 3d, right panel), which unambiguously demonstrates K' valley-locking of the molecules—a hallmark of lattice symmetry protection ensuring robust and stable transport (refer to Supplementary Movies 1 and 2 for time-dependent dynamics and Supplementary Note 3 for more discussions on valley-locking and robustness).

Notably, the boundary engineering technique decouples the molecule transport from the waveguide width (along the y-direction), enabling arbitrary scaling without redesigning the guiding potential (see more details in Supplementary Note 4). This scalability, combined with eigenstate-selective control, establishes a platform for flexible and precise skyrmion manipulation.

Deterministic manipulation of the skyrmion molecules

The boundary engineering method enables selection of eigenstates that match specific boundary conditions. By dynamically tuning these conditions, we can manipulate the skyrmion molecules. In our system, the p-orbital resonant modes and their coupling via the evanescent field depend on the petaloid cavities. Adjusting their geometry can modify the boundary condition (see Supplementary Note 5 for more details). Experimentally, we deploy the dynamic modulation by injecting

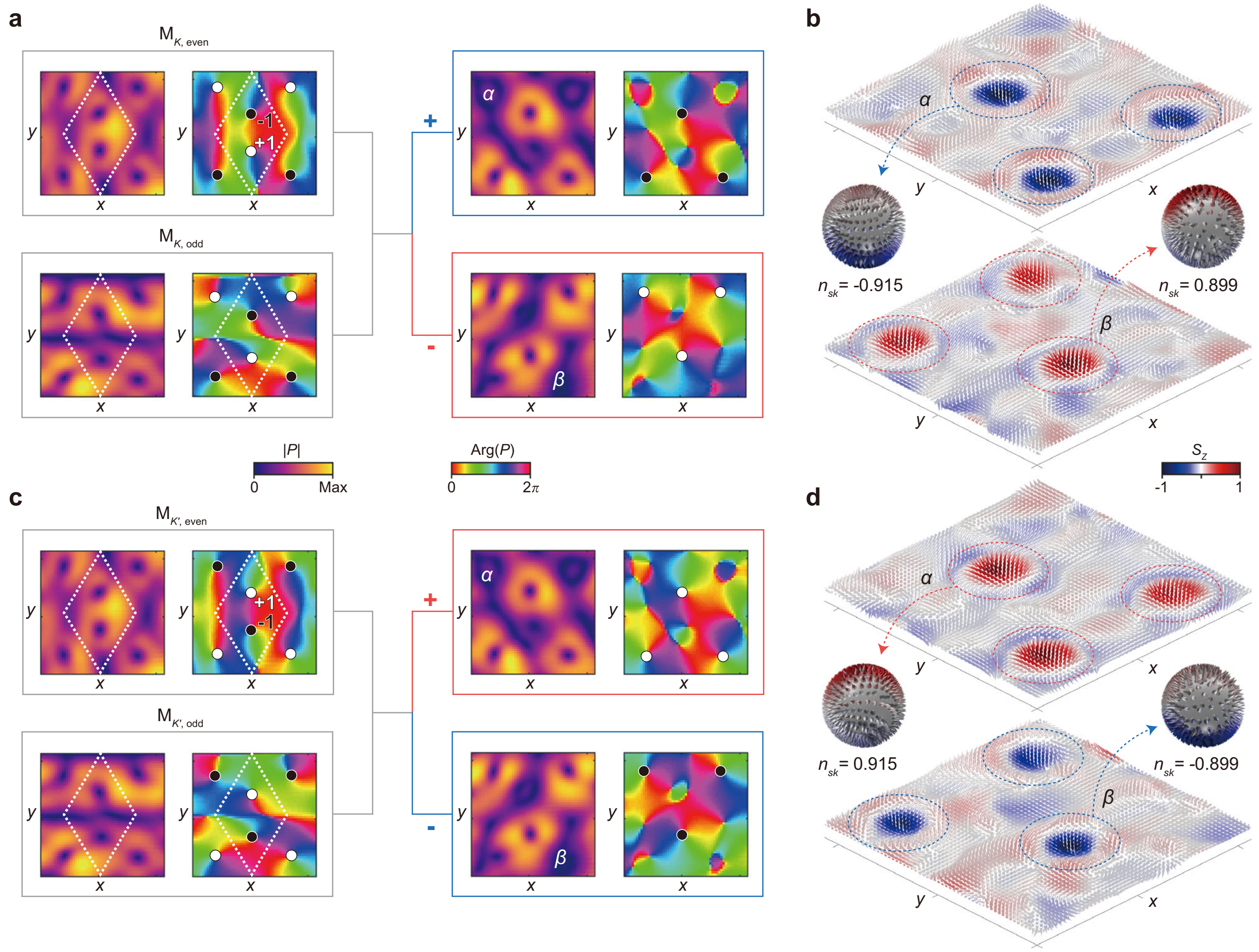

Fig. 5 | Molecule decomposition into individual skyrmion quasiparticles. **a**, **b** Superposition of the even and odd molecules at the K valley. For the scalar pressure field superposition in **a**, experimental data in Figs. 3d and 4d are used, while for the spin vector field superposition in **b**, the data in Figs. 3c and 4c are used. The results demonstrate the decoupling of the vortex/skyrmion pairs, with their individual topological properties isolated at different sublattices. This is corroborated by the quantized skyrmion numbers n_{sk} and the stereographic projections of the spin vector field (within the dashed circular regions). **c**, **d** The same as **a**, **b**, but for the K'-valley decomposition. Parallel analysis reveals time-reversed configurations.

measured amounts of silicone oil into the boundary cavities, as illustrated in Fig. 4a. This changes the cavity depths, leading to a smooth and quantitative control over the skyrmion dynamics. Figure 4b tracks the band structure evolution under such boundary modulation, quantified by the cavity depth change δh. As δh increases, the even skyrmion molecules deform, detach from K and K' valley-locking, and annihilate. At $\delta h = 1.2$ mm, the odd skyrmion molecules emerge with reversed polarizability, as the adjusted boundary condition exclusively selects this eigenstate (see Supplementary Note 5 for more details). Such boundary-engineering-driven mode transition is experimentally validated by the measured band structures in Fig. 4b (colormaps).

To corroborate the band structure observation, we further measure the spin vector and scalar pressure fields under the excitation from the left port of the waveguide at 3.265 kHz (see Fig. 4c, d). Again, stable, uniform molecule lattice configurations are observed. Compared to the even mode in Fig. 3c, d, the spin textures here exhibit reversed polarizability and the vortex pairs display inverted phase winding, matching the $\mathrm{M}_{K,\mathrm{odd}}$ molecule. Like its even counterpart, the odd molecule is also valley-locked, maintaining stability and robustness during propagation, as confirmed by the Fourier analysis (the right panel of Fig. 4d) and the time-dependent transport dynamics (Supplementary Movies 3 and 4). Our boundary engineering technique achieves deterministic control over skyrmion molecules, including their creation, deformation, annihilation and polarizability inversion, with high precision and flexible controllability. Integrating this approach with electro-acoustic or electro-optical couplings could potentially unlock real-time, on-chip skyrmion operations in ultrafast and adaptive spin-wave technologies.

Molecule decomposition

The skyrmion molecules comprise symmetry-locked skyrmion pairs with opposite polarizability, yielding a net topological charge of zero. Despite this neutrality, symmetry protection guarantees that the stable configuration preserves the topological quantization characteristic of individual skyrmions as quasiparticles. To unveil their quasiparticle nature, we superpose the two ground eigenstates of the system, i.e., the even and odd molecules. This decouples the vortex (and therefore the skyrmion) pairs, isolating their properties at each sublattice, as

$$\mathrm{M}_{K,\mathrm{even}} + \mathrm{M}_{K,\mathrm{odd}} \rightarrow \{\Psi_-, 0\}, \quad \mathrm{M}_{K,\mathrm{even}} - \mathrm{M}_{K,\mathrm{odd}} \rightarrow \{0, \Psi_+\}, \tag{4a}$$

for the K valley, and

$$\mathrm{M}_{K',\mathrm{even}} + \mathrm{M}_{K',\mathrm{odd}} \rightarrow \{\Psi_+, 0\}, \quad \mathrm{M}_{K',\mathrm{even}} - \mathrm{M}_{K',\mathrm{odd}} \rightarrow \{0, \Psi_-\}, \tag{4b}$$

for the K' valley.

Figure 5a illustrates the superposition at the K valley using the experimental data in Figs. 3d and 4d. Here, $\mathrm{M}_{K,\,\mathrm{even}}$ is derived by applying the time-reversal operator $\mathscr{T}$ to $\mathrm{M}_{K',\,\mathrm{even}}$, following $\mathrm{M}_{K,\,\mathrm{even}} = \mathscr{T}\mathrm{M}_{K',\mathrm{even}}$. The results show that the sublattice α accommodates vortices with topological charge −1 while β harbors those with +1, consistent with Eq. (4a). Correspondingly, the skyrmion molecules decompose into individual skyrmions, as shown in Fig. 5b. We further calculate their skyrmion numbers n_{sk} using

$$n_{sk} = \frac{1}{4\pi}\iint \hat{\mathbf{s}} \cdot \left(\frac{\partial \hat{\mathbf{s}}}{\partial x} \times \frac{\partial \hat{\mathbf{s}}}{\partial y}\right) dx\,dy, \tag{5}$$

where $\hat{\mathbf{s}} = \mathbf{s}/|\mathbf{s}|$ is the normalized spin vector. Experimental data yield $n_{sk} = -0.915$ at α and $n_{sk} = 0.899$ at β, agreed with the theoretical prediction ∓1 within experimental error (see Methods for error analysis). Superposition at the K' valley is presented in Fig. 5c, d. Due to the time-reversal symmetry, the vortices exhibit exactly reversed chirality compared to the K valley. Concurrently, the skyrmion numbers are inverted, with $n_{sk} = 0.915$ at α and $n_{sk} = -0.899$ at β. These numbers confirm the topological quantization of the skyrmions, revealing their quasiparticle nature and demonstrating the effectiveness of using molecules to stabilize, transport and manipulate skyrmions.

Discussion

We have demonstrated a skyrmion molecule lattice that enables stable transport and precise manipulation, directly addressing critical challenges in skyrmion control. Our method exploits the interactions between anisotropic p-orbitals and Bloch momentum in a designed graphene lattice. The lattice symmetry enforces molecule configurations, which effectively stabilize skyrmions while preserving their topological quasiparticle nature. Compared to existing interference methods relying on tailored excitations, the skyrmion molecules in our system emerge as propagating eigenstates with nonzero group velocity, making them inherently compatible with on-chip integration. More crucially, our boundary engineering technique achieves skyrmion creation, deformation, annihilation, and polarizability inversion. Unlike the nonlinear response of magnetic skyrmions to external fields, our skyrmion molecules have linear dependence on the boundary potential which can be accurately controlled by modulating the boundary condition (see Supplementary Note 5).

Our method for stabilizing, transporting and controlling skyrmions is universal. In terms of lattice symmetry, it can be generalized to other types of point groups or nonsymmorphic symmetries, opening pathways to novel effects like skyrmion Hall effects and non-Abelian skyrmion physics. The orbital basis can also be expanded from p to d, f, or g-orbitals, enabling more sophisticated higher-order spin textures. Furthermore, by leveraging advanced theoretical tools accounting for both global and local topological protection of generalized skyrmions[36,37], richer classes of topological textures can be revealed, not only in various periodic lattices, but also in systems with engineered defects where symmetry, boundary conditions, and singularities might jointly shape the topology.

With the merits of precision and flexibility, the boundary engineering technique can be integrated with active controls such as electro-acoustics, electro-mechanics, or electro-optics, potentially unlocking real-time skyrmion operations in ultrafast and reconfigurable spin-wave technologies. In addition, our method leverages the interaction between vortex lattices and evanescent fields, highlighting the synergy of orbital and spin angular momenta as a scalar-vector duality, which can be important in high-capacity communications, wave-matter interactions, and sensing technologies (see Supplementary Note 6 for an example of using skyrmion molecules to detect the displacement of a small particle, experimentally demonstrating the ability to achieve deep-subwavelength resolution).

Methods

Acoustic cavity and lattice design

Supplementary Fig. S14a and Fig. 2c show the details of the designed acoustic open resonant cavity. The cavity has a radius of $r = 1.5$ cm and a depth of $h_c = 2.2$ cm. The block plates divide the cavity into four sections, with a width of $w = 1.5$ mm, while the circular chamfer has a radius of $r_c = 1.5$ mm. A series of resonant modes within this cavity are identified, as shown in Supplementary Fig. S14b. These modes, including those presented in Fig. 2d, are numerically calculated using the 3D acoustic module of the commercial finite-element software COMSOL Multiphysics under eigenfrequency evaluations. The mass density and sound velocity of air are taken as 1.225 kg/m^3 and 341.7 m/s^1, respectively.

The acoustic lattice, shown in Fig. 2c, is designed with a lattice constant of $a = 3.8\sqrt{3}$ cm. A shallower cavity is chosen to achieve a broader bandwidth for the p-orbital bands, yet most of them are positioned outside the bound region (i.e., above the sound line) (see Supplementary Note 7). To prevent radiation losses, a narrow propagation channel is constructed between the acrylic ceiling and the steel plate (Fig. 2c), with a channel height of $h_a = 1.6$ cm. This design primarily expands the operational bandwidth while maintaining the evanescent wave field, where intensity decays along the out-of-plane direction.

Band structure calculations and measurements

For the acoustic lattice in Fig. 2c, we numerically compute its band structure (Fig. 2e) using COMSOL's 3D acoustic module under eigenfrequency evaluations, considering a single unit cell. Additionally, we calculate the projected band along the x-direction for the finite lattice in Fig. 3a, which has hard boundaries at both ends along the y-direction and periodic boundaries along the x-direction. The results are shown in Fig. 3b. When the depths of the boundary cavities are modified (Fig. 4a), the corresponding projected band structures are presented in Fig. 4b.

Experimentally, the sample is fabricated using metal processing and has a length of $12a$. Two 3D-printed photosensitive resin blocks serve the acoustically hard boundary at both ends of the y-direction (Fig. 3a). The boundary cavity depths are modified by introducing moderate amounts of silicone oil (Fig. 4a), where a depth variation of $\delta h = 1.2$ mm corresponds to 185 µL of silicone oil in each petaloid-shaped small cavity. An acoustic loudspeaker array at the sample's left end excites forward-propagating waves to measure the band structures. For achieving high signal-to-noise ratio measurements, we configure the loudspeaker array to generate even and odd sources, which efficiently stimulate the acoustic fields of even and odd molecule lattices, respectively. A homemade acoustic sensor then scans the middle line (along the x-direction) of the finite sample in discrete steps of a. Data acquisition is performed using a DAQ card (NI 9250 and NI 9234). The collected real-space data are transformed into momentum-space band structures via Fourier transform, with zero-padding employed to enhance resolution. Under different boundary conditions, the measured band structures are presented as color maps in Figs. 3b and 4b.

Acoustic pressure, velocity and spin field measurements

Under excitation by the speaker array at 3.265 kHz, we measure the acoustic velocity and pressure fields using a homemade three-dimensional acoustic particle velocity sensor. This sensor scans the designated region of the finite sample (indicated by the yellow box in Fig. 3a) in 2 mm increments, recording the velocity components $\mathbf{v}\left(v_x, v_y, v_z\right)$ and the acoustic pressure P (for details, see Supplementary Note 8). The measured acoustic velocity and pressure fields are normalized, and the velocity fields are substituted into Eq. (3) to calculate the spin fields $\mathbf{s}$, which is further normalized as $\hat{\mathbf{s}} = \mathbf{s}/|\mathbf{s}|$. The resulting spin fields $\hat{\mathbf{s}}$ are plotted in Fig. 3c for the even mode and Fig. 4c for the odd mode, respectively. The corresponding acoustic pressure distributions are shown in Fig. 3d (even mode) and Fig. 4d (odd mode). The measured acoustic pressure fields are subsequently processed via a two-dimensional Fourier transform to yield the intensity distributions in reciprocal space, illustrated in the right panels of Figs. 3d and 4d. By adding a time-dependent factor $e^{i\omega t}$ into both the acoustic pressure and velocity fields, wave dynamics are visualized in Supplementary Movies 1, 2 (even mode) and 3, 4 (odd mode).

Superpositions of even and odd molecules

Vortex and skyrmion molecules can be decomposed into individual vortices and skyrmions through superpositions, enabling observation of their quantized topological properties. Using the measured acoustic pressure data for the even mode P_{even} (Fig. 3d) and the odd mode P_{odd} (Fig. 4d), we obtain the superpositions at the K and K' valleys as

$$P_{K,\pm} = P^*_{\text{even}} \pm P_{\text{odd}}, \quad P_{K',\pm} = P_{\text{even}} \pm P^*_{\text{odd}}. \tag{M1}$$

The resulting superposed acoustic pressure fields $P_{K,\pm}$ and $P_{K',\pm}$ are shown in Figs. 5a and 5c, respectively. Similarly, the velocity fields are obtained by superposing the measured velocity fields of even mode $\mathbf{v}_{\text{even}}$ and odd mode $\mathbf{v}_{\text{odd}}$ as

$$\mathbf{v}_{K,\pm} = \mathbf{v}^*_{\text{even}} \pm \mathbf{v}_{\text{odd}}, \quad \mathbf{v}_{K',\pm} = \mathbf{v}_{\text{even}} \pm \mathbf{v}^*_{\text{odd}}. \tag{M2}$$

By substituting $\mathbf{v}_{K,\pm}$ and $\mathbf{v}_{K',\pm}$ into Eq. (3), the spin fields are derived, normalized by $\hat{\mathbf{s}} = \mathbf{s}/|\mathbf{s}|$, and shown in Fig. 5b, d. Skyrmion numbers are then computed using Eq. (5), with the integration domain denoted by the dashed circles. The results align with the ideal skyrmion number of ± 1, with only minor discrepancies attributed to experimental errors (see more details in Supplementary Note 9).

Data availability

All data needed to evaluate the conclusions in the paper are present in the paper and/or the Supplementary Materials. The raw data can be accessed on Zenodo at https://doi.org/10.5281/zenodo.17315264.

Code availability

All related codes can be built following the instructions provided in the Methods and Supplementary Information.

References

1. Skyrme, T. H. R. A non-linear field theory. *Proc. R. Soc. A* **260**, 127–138 (1961).
2. Bogdanov, A. N. & Yablonskii, D. A. Thermodynamically stable 'vortices' in magnetically ordered crystals. The mixed state of magnets. *Sov. Phys. JETP* **68**, 101–103 (1989).
3. Rößler, U. K., Bogdanov, A. N. & Pfleiderer, C. Spontaneous skyrmion ground states in magnetic metals. *Nature* **442**, 797–801 (2006).
4. Mühlbauer, S. et al. Skyrmion lattice in a chiral magnet. *Science* **323**, 915–919 (2009).
5. Yu, X. Z. et al. Real-space observation of a two-dimensional skyrmion crystal. *Nature* **465**, 901–904 (2010).
6. Jonietz, F. et al. Spin transfer torques in MnSi at ultralow current densities. *Science* **330**, 1648–1651 (2010).
7. Romming, N. et al. Writing and deleting single magnetic skyrmions. *Science* **341**, 636–639 (2013).
8. Nagaosa, N. & Tokura, Y. Topological properties and dynamics of magnetic skyrmions. *Nat. Nanotechnol.* **8**, 899–911 (2013).
9. Fert, A., Reyren, N. & Cros, V. Magnetic skyrmions: advances in physics and potential applications. *Nat. Rev. Mater.* **2**, 17031 (2017).
10. Bogdanov, A. N. & Panagopoulos, C. Physical foundations and basic properties of magnetic skyrmions. *Nat. Rev. Phys.* **2**, 492–498 (2020).
11. Reichhardt, C., Reichhardt, C. J. O. & Milo, M. V. Statics and dynamics of skyrmions interacting with disorder and nanostructures. *Rev. Mod. Phys.* **94**, 035005 (2022).
12. Hsu, P. J. et al. Electric-field-driven switching of individual magnetic skyrmions. *Nat. Nanotechnol.* **12**, 123–126 (2017).
13. Han, L. et al. High-density switchable skyrmion-like polar nanodomains integrated on silicon. *Nature* **603**, 63–67 (2022).
14. Dai, B. et al. Electric field manipulation of spin chirality and skyrmion dynamic. *Sci. Adv.* **9**, eade6836 (2023).
15. Zhang, S. L. et al. Manipulation of skyrmion motion by magnetic field gradients. *Nat. Commun.* **9**, 2115 (2018).
16. Finazzi, M. et al. Laser-induced magnetic nanostructures with tunable topological properties. *Phys. Rev. Lett.* **110**, 177205 (2013).
17. Yokouchi, T. et al. Creation of magnetic skyrmions by surface acoustic waves. *Nat. Nanotechnol.* **15**, 361–366 (2020).
18. Yang, Y. et al. Acoustic-driven magnetic skyrmion motion. *Nat. Commun.* **15**, 1018 (2024).
19. Koshibae, W. & Nagaosa, N. Creation of skyrmions and antiskyrmions by local heating. *Nat. Commun.* **5**, 5148 (2014).
20. Tsesses, S. et al. Optical skyrmion lattice in evanescent electromagnetic fields. *Science* **361**, 993–996 (2018).
21. Du, L., Yang, A., Zayats, A. V. & Yuan, X. Deep-subwavelength features of photonic skyrmions in a confined electromagnetic field with orbital angular momentum. *Nat. Phys.* **15**, 650–654 (2019).
22. Davis, T. J. et al. Ultrafast vector imaging of plasmonic skyrmion dynamics with deep subwavelength resolution. *Science* **386**, eaba6415 (2020).
23. Dai, Y. et al. Plasmonic topological quasiparticle on the nanometre and femtosecond scales. *Nature* **588**, 616–619 (2020).
24. Lei, X. R. et al. Photonic spin lattices: symmetry constraints for skyrmion and meron topologies. *Phys. Rev. Lett.* **127**, 237403 (2021).
25. Ge, H. et al. Observation of acoustic skyrmions. *Phys. Rev. Lett.* **127**, 144502 (2021).
26. Shen, Y., Hou, Y., Papasimakis, N. & Zheludev, N. I. Supertoroidal light pulses as electromagnetic skyrmions propagating in free space. *Nat. Commun.* **12**, 5891 (2021).
27. Cao, L., Wan, S., Zeng, Y., Zhu, Y. & Assouar, B. Observation of phononic skyrmions based on hybrid spin of elastic waves. *Sci. Adv.* **9**, eadf3652 (2023).
28. Sun, W. J. et al. Localized manipulation of spoof surface acoustic skyrmions with deep-subwavelength gradient structures. *Appl. Phys. Lett.* **122**, 202201 (2023).
29. Hu, P. et al. Observation of localized acoustic skyrmions. *Appl. Phys. Lett.* **122**, 022201 (2023).
30. Kerridge-Johns, W. R., Rao, A. S. & Omatsu, T. Optical skyrmion laser using a wedged output coupler. *Optica* **11**, 769 (2024).
31. Smirnova, D. A., Nori, F. & Bliokh, K. Y. Water-wave vortices and skyrmions. *Phys. Rev. Lett.* **132**, 054003 (2024).
32. Shen, Y. J. et al. Optical skyrmions and other topological quasiparticles of light. *Nat. Photonics* **18**, 15–25 (2024).
33. Zhang, Q. et al. Periodic dynamics of optical skyrmion lattices driven by symmetry. *Appl. Phys. Rev.* **11**, 011409 (2024).
34. Lin, M. et al. Wavelength-tuned transformation between photonic skyrmion and meron spin textures. *Appl. Phys. Rev.* **11**, 021408 (2024).
35. Sun, W. et al. Acoustic skyrmionic mode coupling and transferring in a chain of subwavelength metastructures. *Adv. Sci.* **11**, 2401370 (2024).
36. Wang, A. A. et al. Topological protection of optical skyrmions through complex media. *Light Sci. Appl.* **13**, 314 (2024).
37. Wang, A. A. et al. Generalized skyrmions. Preprint at https://doi.org/10.48550/arXiv.2409.17390 (2024).
38. Wang, B. et al. Topological water-wave structures manipulating particles. *Nature* **638**, 394–400 (2025).

39. Chen, W. N. et al. Observation of multitype topological textures in a subwavelength acoustic Mie resonator. *Phys. Rev. B* **111**, 174302 (2025).
40. He, C. et al. A reconfigurable arbitrary retarder array as complex structured matter. *Nat. Commun.* **16**, 4902 (2025).
41. Bliokh, K. Y. & Nori, F. Spin and orbital angular momenta of acoustic beams. *Phys. Rev. B* **99**, 174310 (2019).
42. Liu, L. et al. Cyclic evolution of synergized spin and orbital angular momenta. *Adv. Sci.* **12**, 2409377 (2025).
43. Rodríguez-Fortuño, F. J. et al. Near-field interference for the unidirectional excitation of electromagnetic guided modes. *Science* **340**, 328–330 (2013).
44. Bliokh, K. Y., Smirnova, D. & Nori, F. Quantum spin Hall effect of light. *Science* **348**, 1448–1451 (2015).
45. Bliokh, K. Y. & Nori, F. Transverse spin and surface waves in acoustic metamaterials. *Phys. Rev. B* **99**, 020301 (2019).
46. Long, Y., Ren, J. & Chen, H. Intrinsic spin of elastic waves. *Proc. Natl. Acad. Sci. USA* **115**, 9951–9955 (2018).
47. Jani, H. et al. Antiferromagnetic half-skyrmions and bimerons at room temperature. *Nature* **590**, 74–79 (2021).
48. Zhang, X. et al. Control and manipulation of a magnetic skyrmionium in nanostructures. *Phys. Rev. B* **94**, 094420 (2016).
49. Yang, S. et al. Reversible conversion between skyrmions and skyrmioniums. *Nat. Commun.* **14**, 3406 (2023).
50. Göbel, B., Mertig, I. & Tretiakov, O. A. Beyond skyrmions: review and perspectives of alternative magnetic quasiparticles. *Phys. Rep.* **895**, 1–28 (2021).
51. Barker, J. & Tretiakov, O. A. Static and dynamical properties of antiferromagnetic skyrmions in the presence of applied current and temperature. *Phys. Rev. Lett.* **116**, 147203 (2016).
52. Griffiths, D. J. & Schroeter, D. F. *Introduction to Quantum Mechanics* (Cambridge University Press, 2018).
53. Wang, M. et al. Valley-locked waveguide transport in acoustic heterostructures. *Nat. Commun.* **11**, 3000 (2020).
54. Liu, L. et al. Width-independent and robust multimode interference waveguides based on anomalous bulk states. *Laser Photonics Rev.* **19**, e00943 (2025).

Acknowledgements

This work are supported by the Key R&D Program of Jiangsu Province [Grant No. BK20232015 (X.J.Z.)], the National Natural Science Foundation of China [Grants Nos. 12222407 (X.J.Z.) and 92363001 (Y.-F. C.)] and the National Key R&D Program of China [Grants Nos. 2023YFA1407700 (X.J.Z.) and 2023YFA1406904 (M.-H.L)].

Author contributions

L.L. and X.J.Z. conceived the idea. L.L. performed the numerical simulation, the theoretical analyses and the experimental measurements. X.J.Z. and L.L. wrote the manuscript. X.J.Z., M.-H.L. and Y.-F.C. supervised all aspects of this work and managed this project.

Competing interests

The authors declare no competing interests.

Additional information

Supplementary information The online version contains supplementary material available at https://doi.org/10.1038/s41467-025-65611-4.

Correspondence and requests for materials should be addressed to Xiujuan Zhang, Ming-Hui Lu or Yan-Feng Chen.

Peer review information *Nature Communications* thanks Hong-Wei Wu and the other anonymous reviewer(s) for their contribution to the peer review of this work. A peer review file is available.

Reprints and permissions information is available at http://www.nature.com/reprints